

**Polarimetric Radar Signatures of a Simulated Supercell Storm
Using a Two-Moment Microphysics Scheme and Polarimetric Radar
Emulator**

Youngsun Jung^{1,2}, Ming Xue^{1,2}, and Guifu Zhang¹

School of Meteorology¹ and Center for Analysis and Prediction of Storms²
University of Oklahoma, Norman OK 73072

Submitted to J. Appl. Meteor. Climatol., 2008

Corresponding author address:
Youngsun Jung
Center for Analysis and Prediction of Storms,
National Weather Center, Suite 2500,
120 David L. Boren Blvd, Norman OK 73072
youngsun.jung@ou.edu

Abstract

A general polarimetric radar emulator is developed based on rigorous scattering calculations using the T-matrix method for reflectivity, differential reflectivity, specific differential phase, and co-polar cross-correlation coefficient. A continuous melting process accounts for the entire spectrum of varying density and dielectric constants. This emulator is able to simulate polarimetric radar measurements at weather radar frequency bands and can take as input the prognostic variables of high-resolution nonhydrostatic NWP model simulations using one-, two-, and three-moment microphysics schemes.

The new emulator is tested at 10.7 cm wavelength with a model-simulated supercell storm using a double-moment (DM, or two-moment) microphysics scheme to examine its ability to simulate polarimetric signatures reported in the observational studies. The simulated fields exhibit realistic polarimetric signatures that include Z_{DR} and K_{DP} columns; Z_{DR} arc, mid-level Z_{DR} and ρ_{hv} rings; and hail signature in terms of the general location, shape and strength. We compared the simulation to one employing a single-moment microphysics scheme and found that certain signatures, such as Z_{DR} arc and mid-level Z_{DR} and ρ_{hv} rings, cannot be reproduced with the latter. It is believed to be primary caused by the lack of proper treatment of size sorting in the single-moment scheme. These results suggest that two- or higher-moment microphysics should be used to adequately describe certain important microphysical processes in supercell storms. They also demonstrate the utility of a well designed radar emulator for validating numerical models. In addition, the simulator can also serve as a training tool for forecasters to recognize polarimetric signatures that can be reproduced by advanced numerical weather prediction models.

1. Introduction

Supercell thunderstorms have received significant attentions from the meteorology community because they often cause serious damage from the associated tornadoes, large hail, strong winds, and/or heavy precipitation. Many observational studies focus mainly on understanding the time evolution of storm structure, microphysical characteristics, and dynamics using radar reflectivity and radial velocity data (e.g., Browning and Donaldson 1963; Browning 1964; Lemon and Doswell 1979; Marwitz 1972; Musil et al. 1986; Ray et al. 1981; Brandes 1978, 1984, 1993). Numerical studies have tried to simulate such supercell storms and aid the understanding of storm evolution and dynamics (e.g., Klemp and Wilhelmson 1978; Klemp et al. 1981; Weisman and Klemp 1982; Rotunno 1981; Klemp and Weisman 1983). Recently, research has demonstrated that the storm microphysical processes and properties can be better understood with polarimetric radar data (e.g., Bringi et al. 1986; Hubbert et al. 1998; Kumjian and Ryzhkov 2008b; a, hereinafter KR08a,b, respectively; Romine et al. 2008).

Although conventional and polarimetric radar observations offer important insights into storms, observations are often insufficient to provide details on the storms due to various limitations. Such limitations include the lack of complete spatial coverage due to beam blockage, radar cone of silence or lack of signal returns in weak echo regions, insufficient temporal frequencies, and insufficient spatial resolution especially when the radar is located far from the storm. In addition to these external factors, reflectivity and polarimetric measurements provide only bulk properties of all hydrometeors in the radar resolution volume, and radial velocity offers only the wind component projected in the direction of the radar beams.

On the other hand, numerical models allow us to study details that are not directly observed by current observational platforms with high temporal and spatial resolutions. They can

help substantiate findings from observational studies. Numerical models also can be used to help develop new theories. Most of all, the numerical model is of primary importance in modern weather forecasting. However, the numerical solutions have to be validated with appropriate observations; there exists a complementary relationship between observations and numerical models.

For direct comparisons between model output and radar observations, the model variables are often converted into the form of observations using the radar emulator, which is also referred to as the forward observation operator in data assimilation terminology. The radar emulator should be accurate, consistent with model microphysics, and make use of all relevant information available in the model.

Most existing polarimetric radar emulators only deal with single-phase hydrometeor concentration (Brandes et al. 1995; Brandes et al. 2004; Ryzhkov et al. 1998; Vivekanandan et al. 1994; Zhang et al. 2001; Capsoni et al. 2001); only a handful of complete polarimetric radar emulators exist in the literature that utilize a full set of parameters available in the numerical model. Huang et al. (2005), in a short conference paper, reported on a simulator based on T-matrix scattering calculations (Waterman 1969; Vivekanandan et al. 1991) using output from the Regional Atmospheric Modeling System (RAMS) employing a two-moment microphysics scheme (Walko et al. 1995; Meyers et al. 1997). In the paper, they employed a simple melting treatment for ice species with fixed fractions of water and ice (and air for graupel) based on the height or air temperature.

Recently, Jung et al. (2008a, hereinafter JZX08) developed a polarimetric simulator combining the power-law fitting of the scattering amplitudes of rain calculated using T-matrix codes and Rayleigh scattering approximation for ice for a single-moment microphysics scheme.

In the work, the authors introduced a new melting ice model with a continuously varying density of ice particles and the fractional water in the ice. For the data assimilation purpose reported in the paper, the emulator had to use curves fitted to pre-calculated data for efficiency; it is therefore not a general purpose emulator.

Pfeifer et al. (2008) also proposed a polarimetric emulator called Synthetic Polarimetric Radar (SynPolRad) based on the T-matrix method. SynPolRad is coupled with a single-moment microphysics scheme with various assumptions about the hydrometeor drop size distributions (DSDs). The authors determined a fixed value for water fraction in wet ice hydrometeors by fitting the values of simulated polarimetric variables to their expected values within a certain range of observations. However, the dielectric constant model used by them is physically questionable because it is based on the assumption of a high-density melting core with a low-density shell. Additionally, the specific differential phase, which is a very useful polarimetric measurement, is not included in SynPolRad.

Although these emulators have their own strengths and weaknesses, they show that polarimetric radar emulators can be useful for evaluating model microphysics. Furthermore, a computationally optimized emulator can serve as a forward observation operator in data assimilation systems.

In this study, we develop a radar emulator that is more general than that described in JZX08 and employs the full T-matrix scattering method for both rain and ice hydrometeors. This emulator allows the specification of any radar wavelength for scattering calculations. In this study, the wavelength is set to 10.7 cm, the wavelength of the U.S. operational Weather Surveillance Radar-1988 Doppler (WSR-88D) radars. Model prognostic variables associated with single-, double-, or three-moment (hereinafter SM, DM, and TM, respectively)

microphysics schemes can be used as inputs. The polarimetric variables simulated include reflectivity at the horizontal and vertical polarizations (Z_H and Z_V), differential reflectivity Z_{DR} , specific differential phase K_{DP} , and the co-polar cross-correlation coefficient at zero-lag $\rho_{hv}(0)$.

A recent study of Dawson et al. (2007; 2009) found that supercell thunderstorms with a more realistic reflectivity structure and cold pool strength can be obtained with a multi-moment microphysics scheme, with most improvement achieved when moving from single-moment to double-moment scheme. In this study, we apply our newly developed emulator to a supercell storm simulated using DM and SM schemes and examine its ability to reproduce characteristic polarimetric signatures commonly found in polarimetric radar observations.

This paper is organized as follows. Section 2 discusses the polarimetric radar data emulator and assumptions about the DSDs. In section 3, the numerical simulation of the supercell storm is described. Section 4 presents the polarimetric radar simulations and the associated polarimetric signatures, and compares them with the results using a SM scheme. The results are summarized in section 5.

2. Polarimetric radar data emulator

The emulator developed in this study is more complex and general than the one reported in JZX08. As discussed in JZX08, the DSD-related parameters within the emulator should be consistent with those used in the numerical model. Within the multi-moment microphysics scheme of Milbrandt and Yau (2005a; 2005b) used in this study and Dawson et al. (2009), the DSDs of each species, $n(D)$, are modeled by a gamma distribution that contain three free parameters,

$$n(D) = N_0 D^\alpha e^{-\Lambda D}, \quad (1)$$

where D is the particle or drop diameter, and N_0 , α , and λ are the intercept, shape, and slope parameters, respectively. Fixed densities of 1,000, 100, 913kg m⁻³ are assumed for rain (ρ_r), snow (ρ_s), and hail (ρ_h), respectively, as in the prediction model.

Additional particle characteristics are needed to simulate polarimetric variables, such as the shape, the statistical properties of the particle orientation, and the ice/water composition of the hydrometeors. Since these parameters are not explicitly specified in the prediction model, assumptions have to be made, based on as much available information as possible. The assumptions we make here are largely inherited from JZX08. Briefly, raindrops, snow aggregates, and hailstones are all assumed as oblate spheroids falling with the major axis aligned horizontally. The oblateness depends on the size of a raindrop while a fixed axis ratio of 0.75 is assumed for snow aggregate and hailstone. The mean canting angles of all hydrometeor types are assumed to be 0°. The standard deviation (SD) of the canting angle are assumed to be 0° for raindrops, 20° for snow aggregates, and a function of the water content in melting hail with maximum 60° for dry hailstones. For more detailed information, the reader is referred to JZX08.

To include the Mie scattering effect for all hydrometeor types, we carry out a numerical integration of the scattering amplitudes over the DSD in the emulator. This enables us to deploy the revised axis ratio relation based on the observations for rain (Brandes et al. 2002),

$$r = 0.9951 + 0.02510D - 0.03644D^2 + 0.005303D^3 - 0.0002492D^4. \quad (2)$$

While a few other relationships, including the ones given by Green (1975) and Beard et al. (1991), are available in the emulator as alternative options, new relationships can easily be added as well.

Within the scattering calculations, the maximum sizes of rain drops ($D_{max,r}$), snow aggregates ($D_{max,s}$), and hailstones ($D_{max,h}$) are assumed to be 8, 30, and 70 mm, respectively.

These size ranges are partitioned into 100 bins. For rain, dry snow, and dry hail, the forward and backward scattering amplitudes along the major and minor axes with assumed drop shape are calculated at the center of each size bin and stored in lookup tables. For melting species, lookup tables are constructed at uniform water fraction intervals, which is 5% in this study. The same melting ice and dielectric constant models developed in JZX08 are employed in the scattering calculation. For example, for a melting snow aggregate with a specified water fraction, the density and dielectric constant of that particle are calculated and used to compute the forward and backward scattering amplitudes at each size bin with that water fraction. These scattering amplitudes are then integrated over the DSD when the model mixing ratios (and the total number concentration for DM and the additional 6th-moment of DSD for TM) are given as input.

For rain, dry snow aggregate, dry hail, rain-snow aggregate mixture, and rain-hail mixture, radar reflectivity factors at horizontal and vertical polarizations are calculated as follows (Zhang et al. 2001):

$$Z_{h,x} = \frac{4\lambda^4}{\pi^4 |K_w|^2} \int_0^{D_{\max,x}} \left[A |f_{a,x}(\pi)|^2 + B |f_{b,x}(\pi)|^2 + 2C \operatorname{Re} [f_{a,x}(\pi) f_{b,x}^*(\pi)] \right] n(D) dD \quad (\text{mm}^6 \text{ m}^{-3}) \quad (3)$$

and

$$Z_{v,x} = \frac{4\lambda^4}{\pi^4 |K_w|^2} \int_0^{D_{\max,x}} \left[B |f_{a,x}(\pi)|^2 + A |f_{b,x}(\pi)|^2 + 2C \operatorname{Re} [f_{a,x}(\pi) f_{b,x}^*(\pi)] \right] n(D) dD \quad (\text{mm}^6 \text{ m}^{-3}) \quad (4)$$

where

$$A = \langle \cos^4 \phi \rangle = \frac{1}{8} \left(3 + 4 \cos 2\bar{\phi} e^{-2\sigma^2} + \cos 4\bar{\phi} e^{-8\sigma^2} \right),$$

$$B = \langle \sin^4 \phi \rangle = \frac{1}{8} \left(3 - 4 \cos 2\bar{\phi} e^{-2\sigma^2} + \cos 4\bar{\phi} e^{-8\sigma^2} \right),$$

and

$$C = \langle \sin^2 \phi \cos^2 \phi \rangle = \frac{1}{8} \left(1 - \cos 4\bar{\phi} e^{-8\sigma^2} \right),$$

and subscript x can be r (for rain) or rs (for rain-snow mixture), ds (for dry snow), rh (for rain-hail mixture), or dh (for dry hail). Here, $f_a(\pi)$ and $f_b(\pi)$ are complex backscattering amplitudes for polarizations along the major and minor axes, respectively, and f_a^* and f_b^* are their respective conjugates. Here, $\text{Re}[\dots]$ represents the real part of the complex number, and $|\dots|$ implies the magnitude of the value between single bars. $\langle \dots \rangle$ means that an ensemble average is taken over canting angles, and $n(D)$ defines the DSD and is the number of particles per unit volume of air and unit bin size. Truncation is applied at maximum sizes of raindrop, snow aggregates, and hailstone when integration over DSD is performed. $\bar{\phi}$ is the mean canting angle, σ is the standard deviation of the canting angle, λ is the radar wavelength, and $K_w = 0.93$ is the dielectric factor for water.

The reflectivity in linear scale for different species are combined to give logarithmic reflectivity at horizontal and vertical polarizations (Z_H and Z_V , respectively) and differential reflectivity (Z_{DR}) as according to

$$Z_H = 10 \log_{10} \left(Z_{h,r} + Z_{h,rs} + Z_{h,ds} + Z_{h,rh} + Z_{h,dh} \right) \text{ dBZ}, \quad (5)$$

$$Z_V = 10 \log_{10} \left(Z_{v,r} + Z_{v,rs} + Z_{v,ds} + Z_{v,rh} + Z_{v,dh} \right) \text{ dBZ}, \quad (6)$$

$$Z_{DR} = 10 \log_{10} \left(\frac{Z_h}{Z_v} \right) = 10 \log_{10} \left(\frac{Z_{h,r} + Z_{h,rs} + Z_{h,ds} + Z_{h,rh} + Z_{h,dh}}{Z_{v,r} + Z_{v,rs} + Z_{v,ds} + Z_{v,rh} + Z_{v,dh}} \right) \text{ dB}. \quad (7)$$

Z_{DR} is a good indicator of the mean shape of hydrometeors and depends on their relative orientation to the radar beam. Therefore, DSD changes toward larger or smaller drop sizes can be roughly inferred from the Z_{DR} value.

The cross-correlation coefficient is defined as

$$\rho_{hv} = \frac{|Z_{hv,r} + Z_{hv,s} + Z_{hv,h} + Z_{hv,rs} + Z_{hv,rh}|}{\left\{ (Z_{h,r} + Z_{h,s} + Z_{h,h} + Z_{h,rs} + Z_{h,rh})(Z_{v,r} + Z_{v,s} + Z_{v,h} + Z_{v,rs} + Z_{v,rh}) \right\}^{1/2}}, \quad (8)$$

where the numerator is given as a product of two orthogonal co-polar components of the radar signals and computed as

$$Z_{hv,x} = \frac{4\lambda^4}{\pi^4 |K_w|^2} \int_0^{D_{\max,x}} \left[C(|f_{a,x}(\pi)|^2 + |f_{b,x}(\pi)|^2) + A(f_{a,x}(\pi)f_{b,x}^*(\pi)) + B(f_{b,x}(\pi)f_{a,x}^*(\pi)) \right] n(D)dD \quad (\text{mm}^6 \text{ m}^{-3}). \quad (9)$$

Cross-correlation coefficient ρ_{hv} is very useful in detecting the melting layer since it is sensitive to the presence of water-ice mixtures. For example, ρ_{hv} is very high for pure rain but is much lower in the presence of randomly oriented, large, wet hailstones.

The specific differential phases for rain, rain-snow aggregate mixture, and dry snow aggregate, rain-hail mixture, and dry hail are calculated according to

$$K_{DP,x} = \frac{180\lambda}{\pi} \int_0^{D_{\max,x}} C_k \text{Re}[f_{a,x}(0) - f_{b,x}(0)] n(D)dD \quad (^\circ \text{ km}^{-1}), \quad (10)$$

where

$$C_k = \langle \cos 2\phi \rangle = \cos 2\bar{\phi} e^{-2\sigma^2}$$

and $f_a(0)$ and $f_b(0)$ are forward scattering amplitudes for polarizations along the major and minor axes, respectively. K_{DP} is known as more useful in quantitative precipitation estimation because it is more linearly proportional to the rainfall rate than reflectivity. However, the K_{DP} field is often very noisy in weak rain regions and vulnerable to errors.

When creating observations on the radar elevation planes, the effective earth radius model (Doviak and Zrnic 1993) is used to take into account beam bending and a Gaussian beam

weighting function described in Xue et al. (2006) is used in the vertical direction. The error model described in Xue et al. (2007) and Jung et al. (2008b) is optional for adding simulated observations errors. In this study, error-free polarimetric variables are created at each grid points.

3. Numerical simulation

Similar to the truth simulation used in (Jung et al. 2008b, hereafter JXZS08), an idealized supercell storm is initialized by a thermal bubble placed in a horizontally homogeneous environmental defined by the sounding of the May 20, 1977 Del City, Oklahoma, supercell storm (Ray et al. 1981). The storm is simulated using the Advanced Regional Prediction System (ARPS, Xue et al. 2000; 2001; 2003), which is a fully compressible and non-hydrostatic atmospheric prediction model. The multi-moment bulk microphysics scheme of Milbrandt and Yau (2005a; 2005b, hereinafter MY05) is recently implemented in the ARPS (Dawson II et al. 2007; Dawson II et al. 2009) and is used in this study.

With the DM option, the ARPS predicts three velocity components u , v , and w ; potential temperature θ ; pressure p ; mixing ratios of water vapor q_v ; and mixing ratios of cloud water, rainwater, cloud ice, snow aggregate, and hail (q_c , q_r , q_i , q_s , and q_h , respectively), and their total number concentrations (N_{t_c} , N_{t_r} , N_{t_i} , N_{t_s} , and N_{t_h} , respectively). The graupel category originally included in the MY05 package is turned off to maintain consistency with our previous experiments (JXZS08 and JXZ08). The turbulence kinetic energy is also predicted by the model and is used in the 1.5-order subgrid-scale turbulence closure scheme.

The initiating bubble has an ellipsoidal shape and has 4-K maximum temperature perturbation, and is 10 km long and 1.5 km high, and centered at $x = 48$ km, $y = 16$ km, and $z = 1.4$ km in a $63 \times 63 \times 16$ km³ model domain. Radiation, rigid wall with a wave-absorbing layer, and free-slip condition are applied to the lateral, top, and bottom boundaries, respectively.

A few changes are made to the configurations used in JXZS08 and JXZ08 to accommodate the use of DM. The horizontal grid spacing used is 1.5 km and the vertical grid spacing is 0.5 km. A higher horizontal resolution is used here because the model fails to simulate storm splitting at a 2 km resolution with the double-moment scheme. Constant winds of $u = 1 \text{ m s}^{-1}$ and $v = 13 \text{ m s}^{-1}$ are subtracted from the original sounding to keep the storm near the center of the domain. The time step size is 3 seconds for the general model integration and 1.5 seconds for acoustic modes. A 4th-order monotonic computational mixing (Xue 2000) is used to prevent Gibbs phenomenon.

The multi-moment bulk microphysics of MY05 assumes that each hydrometeor type has a constant density. The default values for rain, snow, and hail are 1,000, 100, and 913 kg m^{-3} but can be altered by the user. The DSDs for all hydrometeor types are modeled by exponential distribution in the current study.

4. Simulated polarimetric signatures

a. Storm evolution and simulated reflectivity

Figure 1 shows the time evolution of the reflectivity and other fields of the simulated supercell storm using SM and DM microphysics schemes of MY05, at 250 m altitude. Briefly, the updraft quickly intensifies during the first 20 minutes, with a reflectivity core greater than 40 dBZ appearing after 10 minutes of simulation (not shown). While the forward flank regions continue to expand in the next 30 minutes, the storm starts to split into two cells at around 1 hour (Fig. 1f). The left-moving cell (relative to the environmental shear vector) then continues to develop while propagating to the northwest of the right-moving cell. The right-moving cell is at its mature stage by 80 min of model time and maintains its intensity for the next few hours. In this study, we focus on the right-moving storm, which is usually the dominant one.

As discussed in Dawson et al. (2007; 2009), though for a different case, the simulated reflectivity using DM (Figs. 1e-h) shows a more realistic structure and intensity in the hook echo and forward flank downdraft (FFD) regions compared to the results of SM scheme (Figs. 1a-d). Our simulated storm using MY05 SM scheme is very similar to that using the Lin et al. (1983, hereafter LFO83) ice microphysics scheme shown in Fig. 2 of TX05, with the same Del City sounding. Compared to the echo obtained with DM scheme, that using SM one has a kidney shape with a narrow FFD, while DM produces a swirl-shaped weak echo region (WER) wrapping around the hook echo and extends the FFD to the far east of the storm (Figs. 1d, h). Another significant difference between the storms using SM and DM schemes is in the cold pool strength. A SM scheme with default DSD parameter settings tends to produce a stronger cold pool than a DM scheme. Dawson et al. (2008) showed that one of the main causes of the strong cold pool with SM scheme is the evaporative cooling of raindrops in the downdraft related to the fixed, large, N_{or} , which is related to a larger number of small drops that can evaporate quickly.

A detailed evaluation of microphysics schemes is beyond the scope of this study. Our focus will be on the ability of our emulator in reproducing characteristic polarimetric signatures when using different microphysics schemes.

b. Simulated polarimetric radar variables

Several unique polarimetric signatures have been reported in observational studies of supercell storms. They include strong Z_{DR} and K_{DP} columns, a mid-level Z_{DR} ring, a hail signature (Z_{DR} hole), Z_{DR} arc (Z_{DR} shield), and mid-level ρ_{hv} ring (e.g., Wakimoto and Bringi 1988; Bringi et al. 1986; Hubbert et al. 1998; Kumjian and Ryzhkov 2008b; a, hereafter KR08a and b; Romine et al. 2008). These signatures appear in the specific locations within a storm as a result of storm dynamics and microphysics. If the numerical model can handle the related storm

dynamics and microphysics properly, a realistic polarimetric radar emulator should be able to reproduce those signatures. In this study, the ability of our simulator in reproducing individual signatures is examined in the following subsections.

1) Z_{DR} and K_{DP} columns

Figure 2 shows the vertical structures of Z_{DR} (Fig. 2a) along line AA' in Fig. 1h, and of K_{DP} (Fig. 2b) along line BB'. Both cross-sections pass through the maximum vertical velocity region within the storm. The locations of the Z_{DR} and K_{DP} columns are associated with the updraft because super-cooled rainwater is carried aloft by a strong updraft and often tilted in vertically sheared environments (Fig. 2). The Z_{DR} and K_{DP} columns extending above 0°C level are clear in Fig. 2. As reported in the observational study of Ryzhkov et al. (2005), the K_{DP} column is associated with the rear-flank downdraft (RFD) region near the surface (not shown).

An offset in the centers of K_{DP} and Z_{DR} columns is pointed out by KR08a in their observational study of polarimetric signatures. In the observations, the K_{DP} column is often found west or northwest of the Z_{DR} column. A similar offset is observed in the lower mid-levels (Figs. 3a,d) in our simulation, while they become collocated at the upper mid-levels (Figs. 3c,f). At the 3 km altitude, the Z_{DR} column is located south of the updraft core near the reflectivity hook. This agrees well with the location of Z_{DR} column reported in Hubbert et al. (1998). At this level, the K_{DP} column is found at the reflectivity maximum and in the west part of the updraft core. At the 4-km altitude, the Z_{DR} column appears as a half-ring wrapping around the updraft core on the east side (Fig. 3b), while the center of the K_{DP} column is moving toward the updraft core (Fig. 3e). At the 5 km height, the Z_{DR} and K_{DP} columns are almost collocated with the updraft core (Figs. 3e,f). The offset in the centers is also found in the SM run but the amount of offset is less than that of the DM run's (not shown).

The main cause of the offset of the Z_{DR} column from the updraft core is the presence of hail. From Figs. 3g,h,i, it is apparent that the production of q_r is strongly related to the updraft. Within the updraft, the low-level q_r is transported to the higher level, and q_r is also created through in-situ condensation and autoconversion from cloud water. q_h is also produced in the updraft. Large hailstones fall through the updraft, and small hailstones are carried out of the updraft while growing and falling in the FFD region north of the updraft core. The high q_h region overlaps with the high q_r region in the north or northwest. The presence of hail reduces the Z_{DR} because the tumbling nature of the hailstones that makes their apparent shape close to spherical. Therefore, high Z_{DR} column shows up at the south or southeast side of the updraft.

On the other hand, the K_{DP} is almost transparent to the hail and is only sensitive to the amount of rainwater. The K_{DP} maximum, high q_r region, and updraft core are, hence, almost collocated.

2) Z_{DR} arc

The Z_{DR} arc is the low-level signature often observed at the southern edge of FFD along the sharp gradient zone of reflectivity in right-moving supercells (KR08a). This is characterized by a horizontally elongated high Z_{DR} band along the right edge of the FFD near the surface. Although a quite common feature in supercells, regardless of season or geographic region, this signature has not been noted until recently (KR08a,b, Romine et al. 2008). This signature is analyzed in detail in KR08b, where it is argued that the size sorting mechanism, due to strong wind speed and directional shears, is primarily responsible for this signature; large drops discharged from the updraft fall into the region close to the origin, while smaller drops are advected farther into the FFD. The rain evaporation is likely another source of a modified DSD toward a large D_{nr} (Dawson et al. 2009). In the location of Z_{DR} arc, the DSD, initially lacking

small drops, loses small drops fast due to evaporation while falling through dry air. To properly model such processes responsible for DSD changes, a two- or higher moment microphysics scheme has to be used; a SM scheme is not capable of handling such mechanisms (Fig. 4a, Dawson et al. 2009).

The modified DSD of rain as a result of the size sorting can be evaluated easily by examining the mean-mass diameter D_{nr} , where the D_{nr} is calculated for the exponential distribution as

$$D_{nr} = \left(\frac{q_r \rho_{air}}{\pi \rho_r N t_r} \right)^{1/3}, \quad (10)$$

where ρ_{air} is the density of air. For a SM scheme, D_{nr} is dependent only on q_r because $N t_r = N_{0r} D_{nr}$, where N_{0r} is a constant. The DSD directly affects Z_{DR} because Z_{DR} is proportional to the median diameter of precipitation particles in the radar resolution volume. The calculated D_{nr} for SM and DM is presented in Fig. 4 along with simulated Z_{DR} .

The Z_{DR} arc signature is well captured by the DM scheme and polarimetric radar data emulator at a 0.5 km altitude at 80 min of simulated storm in Fig. 4b. The high Z_{DR} region along the southern edge of the FFD is shallow (~ 2 km deep), rather narrow, but persistent in time, as observed, and it shifts slightly toward the north with height. The arc band becomes weak and broad above 2 km, practically fading away. The shape and location of the high Z_{DR} region match the D_{nr} pattern. The q_r pattern, in conjunction with that of D_{nr} , designates this area as having a small number of large drops and lacking small drops. On the other hand, the simulated storm using the SM scheme completely misses the Z_{DR} arc signature because both D_{nr} and Z_{DR} are proportional only to rainwater mixing ratio q_r (Fig. 4a).

3) Mid-level Z_{DR} and ρ_{hv} rings

The mid-level Z_{DR} ring (KR08a) refers to the enhanced Z_{DR} in the shape of a ring with a depressed Z_{DR} value in the middle. The Z_{DR} ring is sometimes a complete circle and sometimes just a half-ring. KR08a reports that the enhanced Z_{DR} region is always found on the right flank of the updraft when only a half-ring is manifested. In our simulation, it is usually a half-ring on the right flank of the updraft at the mid-levels and close to a complete ring in the lower levels.

The half- Z_{DR} ring in Fig. 5a mostly overlaps with the high D_{nr} region. The maximum D_{nr} region is collocated with the updraft core. The local maxima found on the south and east sides of the main D_{nr} core may be explained by large raindrops falling around the updraft following a cyclonic circulation (associated with a cyclonically rotating updraft, Fig. 3d-f). The missing half of the ring signature is highly correlated with the presence of hail (Fig. 5a). As discussed in earlier subsection 1), the presence of hailstones reduces the Z_{DR} values because their tumbling motion and random orientation make their apparent shape spherical to radar beams. At the 4 km altitude, the region with high hail-mixing ratios is located to the west and northwest of the updraft core. This weakens the Z_{DR} signature on the left flank of the updraft.

The ρ_{hv} ring is another mid-level feature with depressed (instead of increased) ρ_{hv} values in a ring pattern (KR08a). A well-defined ρ_{hv} ring is seen in Fig. 5b. The ρ_{hv} values for pure water and ice are very high but decrease when hydrometeors of diverse types are mixed together. The dotted contours in Fig. 5b show the ratio of rain-hail mixture to the rain and dry hail total mixing ratio. High values of this ratio indicate the presence of three different types, with the mixture being dominant in the regions of ρ_{hv} ring. The low values of the ratio suggest either pure rain or dry hail is dominant [see Eq. (2) and section 3b of JZX08 for more details on the melting ice model used here]. The pattern of this ratio agrees well with the ring-shaped ρ_{hv} depression.

When ice is in a melting phase, the resonance effect due to Mie scattering can contribute to the reduction of ρ_{hv} (Fig. 6), which occurs when the ratio $D|\varepsilon|^{1/2}/\lambda$ approaches 1 (KR08a,b), where ε is the dielectric constant. For dry hail, ρ_{hv} slowly decreases with size within the range shown in Fig. 6, in which the particle size is truncated at 42.35 mm. With the given exponential DSD, large drops have little effect because the number of drops is very small at that size, although the resonance effect can be much more significant in very large drops. It can be seen that the ρ_{hv} shows a sudden drop at a certain size. Both the characteristic size and maximum amplitude decrease with increasing water fraction. The size sorting mechanism is also necessary to simulate this signature; so that the DSD can have a sufficient number of hailstones at the characteristic size to reduce the total ρ_{hv} values. This signature is very weak or completely missing when an SM is used (not shown).

We would like to point out that the simulated ρ_{hv} is higher than the typically observed values. Non-meteorological effects that can also contribute to the reduction of ρ_{hv} , such as noise bias, clutter contamination, dust and bugs, are not included in our emulator. These may partially be responsible for the rather high ρ_{hv} in our simulation. Another source of difference might be the simplified model of randomly orientated spheroids for hail and snow, which does not account for the effect of irregular shapes of natural hydrometeors.

4) *Hail signature in the forward flank downdraft*

The observed hail signature is characterized by a high Z_H and low Z_{DR} at the lowest radar elevation associated with hail reaching the ground (KR08a). This feature is also called “ Z_{DR} -Hole” (Wakimoto and Bringi 1988), which often stretches from the surface up to a certain height. Our simulated storm does not exhibit this signature near the surface because most of the hail completely melts while falling in this area. However, the emulator is capable of simulating this

signature if a significant amount of hail survives the melting and reaches the ground. For example, a hail signature is evident at a 2.5 km height, where a relatively large hail concentration is present (Fig. 7). The simulated Z_{DR} pattern with a Z_{DR} -Hole surrounded by high Z_{DR} values shows a remarkable similarity to the observation shown in Fig. 3a of KR08a.

5. Summary and discussions

In this paper, a synthetic polarimetric radar emulator based on full T-matrix scattering calculations and accurate formulations for polarimetric radar variables is developed. This emulator takes advantage of the continuous melting ice model developed in Jung et al. (2008a, hereinafter JZX08). The density of the melting ice and dielectric constant are also allowed to vary continuously. This emulator can specify any weather radar wavelength and use up to three moments of microphysics parameterization, i.e., the total number concentrations, mixing ratios and reflectivity factors of multiple hydrometeors, as input.

This emulator can simulate the reflectivity of the horizontal and vertical polarizations (Z_H and Z_V), differential reflectivity (Z_{DR}), specific differential phase (K_{DP}), and cross-correlation coefficient (ρ_{hv}) as well as radial velocity (V_r). These quantities are what will be observed by operational WSR-88D radars after the polarimetric upgrade and are currently being measured by the prototype polarimetric WSR-88D radar located at Norman Oklahoma, the KOUN radar.

The new radar emulator is applied to an idealized supercell storm simulated using a two- or double-moment (DM) microphysics scheme. Another storm with the same configurations but using a single-moment (SM) microphysics scheme is created for comparison. The simulated storm using a DM scheme exhibits unique polarimetric signatures reported in the literature, including the Z_{DR} and K_{DP} columns, Z_{DR} arc, mid-level Z_{DR} and ρ_{hv} rings, and hail signature. Some of the signatures, mostly related to the size sorting mechanisms, however, could not be

simulated when a SM scheme was used. These signatures include the Z_{DR} arc and mid-level Z_{DR} and ρ_{hv} rings. These results support that a two- or higher-moment microphysics scheme has to be used to properly describe these important aspects of thunderstorms. Properly simulating these processes are also important to effectively assimilate polarimetric data into numerical models for initialization purpose.

To evaluate the fidelity of our simulator, we compared the above signatures to those simulated using the simple emulator developed in JZX08, where efficiency was given an equal weight when it was developed for data assimilation purposes. The simulator of JZX08 is found to simulate most of the signatures. However, the Z_H , Z_{DR} , and K_{DP} values are somewhat higher than observations because of the choice of the axis ratio to avoid numerical integration. And the ρ_{hv} ring could not be simulated correctly because the Mie scattering for the ice species is not included there (Fig. 8).

The verification of convective-scale numerical weather prediction is challenging because most of the model variables are not directly observed at this scale. Radar reflectivity has been used to verify the model prediction for a while. However, reflectivity alone is insufficient to verify microphysics because many independent variables and uncertain constants based on many assumptions on drop size distributions (DSDs) are involved in reflectivity calculation. Here, simulated polarimetric variables can help discriminate against and/or highlight certain variables from others by using their differential sensitivity to the water phases. They can be as useful as reflectivity because they contain additional information on the DSDs and microphysical processes. As an example, JXZ08 demonstrated that a realistic radar simulator could be useful in evaluating the model microphysics scheme by identifying delayed melting processes in the Lin-

type microphysics scheme. Additionally, a realistic simulator could provide an opportunity to study storm microphysical processes in more depth.

A good radar simulator can also help forecasters to determine where attention and monitoring should be directed in a high threat situation, given convective-scale model output. Kumjian and Ryzhkov (2008a) related some of the polarimetric signatures to the severity of the storms: the stronger the updraft in developing storms, the stronger the Z_{DR} and K_{DP} columns, and the stronger the enhanced storm-relative environmental helicity (SREH), the stronger the Z_{DR} arc signature. This suggests that polarimetric signatures can be used as an indicator of storm intensity. Although the numerical model provides the vertical velocity as one of the prognostic variables, observed quantities can often be interpreted more intuitively. For instance, analyzing the Z_{DR} field could be as informative as examining the mixing ratio and the number concentration of each hydrometeor type separately in addition to the vertical velocity field. In this regard, the polarimetric emulator can be useful to the forecasters by providing the opportunity to look at the model polarimetric fields in advance of the occurrence of the actual event.

Another potential for the practical use of the simulator is for it to serve as a guide to the design of future assimilation systems. The results presented in this paper suggest that assimilating Z_{DR} will likely increase the analysis error when a single-moment microphysics scheme is used in the forecast model. For example, when a SM scheme is used, the only way to simulate the Z_{DR} arc is to increase the rainwater mixing ratio at the southern edge of the forward flank downdraft when the Z_{DR} data are assimilated. However, this would increase the reflectivity in that area, which conflicts with what the observed reflectivity shows. These results suggest that

it may be better not to assimilate Z_{DR} data when a SM scheme is used in the prediction model. This is an area require further study.

For higher frequency such as the X-band radars, attenuation from the severe storm can be significant enough to alter observed polarimetric signatures, which are very different from the theoretical ones. In this case, an attenuation algorithm must be included to produce realistic polarimetric signatures. This will be developed as a part of the emulator in the future while a simplified version already exists in a data assimilation framework (Xue et al. 2009). The evaluation of both multi-moment microphysics scheme and the simulator using KOUN data is also planned for the future.

Acknowledgement: The authors thank Matthew Kumjian for useful discussions on the interpretation of observed polarimetric signature. The authors also thank Dr. Jason Milbrandt and Daniel Dawson for helping us to use a multi-moment microphysics scheme. The original T-matrix code was provided by Dr. J. Vivekanandan. This work was primarily supported by NSF grants EEC-0313747 and ATM-0608168. Ming Xue was also supported by NSF grants ATM-0530814, ATM-0802888, ATM-0331594 and ATM-0331756. The computations were performed at the OU Supercomputing Center for Education and Research.

References

- Beard, K. V., R. J. Kubesh, and H. T. Ochs, 1991: Laboratory measurements of small raindrop distortion. Part I: Axis ratios and fall behavior. *J. Atmos. Sci.*, **48**, 698-710.
- Brandes, E. A., 1978: Mesocyclone evolution and tornadogenesis: Some observations. *Mon. Wea. Rev.*, **106**, 995-1011.
- Brandes, E. A., 1984: Vertical vorticity generation and mesocyclone sustenance in tornadic thunderstorms: The observational evidence. *Mon. Wea. Rev.*, **112**, 2253-2269.
- Brandes, E. A., 1993: Tornadic thunderstorm characteristics determined with Doppler radar. In *The Tornado: Its Structure, Dynamics, Prediction and Hazards, Geophys. Monogr.*, Amer. Geophys. Union, 143-159.
- Brandes, E. A., G. Zhang, and J. Vivekanandan, 2002: Experiments in rainfall estimation with a polarimetric radar in a subtropical environment. *J. App. Meteor.*, **41**, 674-685.
- Brandes, E. A., G. Zhang, and J. Vivekanandan, 2004: Comparison of polarimetric radar drop size distribution retrieval algorithms. *Journal of Atmospheric and Oceanic Technology*, **21**, 584-598.
- Brandes, E. A., J. Vivekanandan, J. D. Tuttle, and C. J. Kessinger, 1995: A study of thunderstorm microphysics with multiparameter radar and aircraft observations. *Mon. Wea. Rev.*, **123**, 3129-3143.
- Bringi, V. N., R. M. Rasmussen, and J. Vivekanandan, 1986: Multiparameter radar measurements in Colorado convective storms. Part I: Graupel melting studies. *J. Atmos. Sci.*, **43**, 2545-2563.
- Browning, K. A., 1964: Airflow and precipitation trajectories within severe local storms which travel to the right of the mean winds. *J. Atmos. Sci.*, **21**, 634-639.

- Browning, K. A. and R. J. Donaldson, 1963: Airflow and structure of a tornadic storm. *J. Atmos. Sci.*, **20**, 533-545.
- Capsoni, C., M. D'Amico, and R. Nebuloni, 2001: A Multiparameter polarimetric radar simulator. *Journal of Atmospheric and Oceanic Technology*, **18**, 1799-1809.
- Dawson II, D. T., M. Xue, and J. A. Milbrandt, 2008: Improvements in the treatment of evaporation and melting in multi-moments versus single-moment bulk microphysics: results from numerical simulations of the 3 May 1999 Oklahoma tornadic storms. 24th Conf. Severe Local Storms
- Dawson II, D. T., M. Xue, J. A. Milbrandt, and M. K. Yau, 2009: The effects of evaporation and melting in a multi-moment bulk microphysics scheme on the low-level downdrafts and surface cold pools in the simulations of the 3 May 1999 Oklahoma tornadic thunderstorms. *Mon. Wea. Rev.*, Submitted.
- Dawson II, D. T., M. Xue, J. A. Milbrandt, M. K. Yau, and G. Zhang, 2007: Impact of multi-moment microphysics and model resolution on predicted cold pool and reflectivity intensity and structures in the Oklahoma tornadic supercell storms of the 3 May 1999. 22nd Conf. Num. Wea. Pred.
- Doviak, R. and D. Zrnic, 1993: *Doppler Radar and Weather Observations*. 2nd ed. Academic Press, 562 pp.
- Green, A. V., 1975: An approximation for shape of large raindrops. *J. Appl. Meteor.*, **14**, 1578-1583.
- Huang, G.-J., V. N. Bringi, S. v. d. Heever, and W. Cotton, 2005: Polarimetric radar signatures from RAMS microphysics. 32nd Int. Conf. Radar Meteor., Albuquerque, NM, Amer. Meteor. Soc., CDROM P11R.6.

- Hubbert, J., V. N. Bringi, L. D. Carey, and S. Bolen, 1998: CSU-CHILL polarimetric radar measurements from a severe hail storm in eastern Colorado. *Journal of Applied Meteorology*, **37**, 749-775.
- Jung, Y., G. Zhang, and M. Xue, 2008a: Assimilation of simulated polarimetric radar data for a convective storm using ensemble Kalman filter. Part I: Observation operators for reflectivity and polarimetric variables. *Mon. Wea. Rev.*, **136**, 2228-2245.
- Jung, Y., M. Xue, G. Zhang, and J. Straka, 2008b: Assimilation of simulated polarimetric radar data for a convective storm using ensemble Kalman filter. Part II: Impact of polarimetric data on storm analysis. *Mon. Wea. Rev.*, **136**, 2246-2260.
- Klemp, J. B. and R. B. Wilhelmson, 1978: Simulations of right- and left-moving thunderstorms produced through storm splitting. *J. Atmos. Sci.*, **35**, 1097-1110.
- Klemp, J. B. and M. L. Weisman, 1983: The dependence of convective precipitation patterns on vertical wind shear. Preprints, 21st Conf. on Radar Meteorology, Edmonton, Amer. Meteor. Soc., 44-49.
- Klemp, J. B., R. B. Wilhelmson, and P. S. Ray, 1981: Observed and numerically simulated structure of a mature supercell thunderstorm. *J. Atmos. Sci.*, **38**, 1558-1580.
- Kumjian, M. R. and A. V. Ryzhkov, 2008a: Storm-relative helicity revealed from polarimetric radar measurements. *J. Atmos. Sci.*, In print.
- Kumjian, M. R. and A. V. Ryzhkov, 2008b: Polarimetric signatures in supercell thunderstorms. *J. Appl. Meteor. Climatol.*, **47**, 1940-1961.
- Lemon, L. R. and C. A. Doswell, 1979: Severe thunderstorm evolution and mesocyclone structure as related to tornadogenesis. *Mon. Wea. Rev.*, **107**, 1184-1197.

- Lin, Y.-L., R. D. Farley, and H. D. Orville, 1983: Bulk parameterization of the snow field in a cloud model. *J. Climate Appl. Meteor.*, **22**, 1065-1092.
- Marwitz, J. D., 1972: The structure and motion of severe hailstorms. Part I: Supercell storms. *J. Appl. Meteor.*, **11**, 166-179.
- Meyers, M. P., R. L. Walko, J. R. Harrington, and W. R. Cotton, 1997: New RAMS cloud microphysics parameterization. Part II: The two-moment scheme. *Atmos. Res.*, **45**, 3-39.
- Milbrandt, J. A. and M. K. Yau, 2005a: A multi-moment bulk microphysics parameterization. Part I: Analysis of the role of the spectral shape parameter. *J. Atmos. Sci.*, **62**, 3051-3064.
- Milbrandt, J. A. and M. K. Yau, 2005b: A multi-moment bulk microphysics parameterization. Part II: A proposed three-moment closure and scheme description. *J. Atmos. Sci.*, **62**, 3065-3081.
- Musil, D. J., A. J. Heymsfield, and P. L. Smith, 1986: Microphysical characteristics of a well-developed weak echo region in a High Plains supercell thunderstorm. *J. Climate Appl. Meteor.*, **25**, 1037-1051.
- Pfeifer, M., G. C. Craig, M. Hagan, and C. Keil, 2008: A polarimetric radar forward operator for model evaluation. *J. Appl. Meteor. Climatol.*, DOI: 10.1175/2008JAMC1793.1.
- Ray, P. S., B. Johnson, K. W. Johnson, J. S. Bradberry, J. J. Stephens, K. K. Wagner, R. B. Wilhelmson, and J. B. Klemp, 1981: The morphology of severe tornadic storms on 20 May 1977. *J. Atmos. Sci.*, **38**, 1643-1663.
- Romine, G. S., D. W. Burgess, and R. B. Wilhelmson, 2008: A dual-polarization-radar-based assessment of the 8 May 2003 Oklahoma City area tornadic supercell. *Mon. Wea. Rev.*, **136**, 2849-2870.
- Rotunno, R., 1981: On the evolution of thunderstorm rotation. *Mon. Wea. Rev.*, **109**, 171-180.

- Ryzhkov, A. V., D. S. Zrnica, and B. A. Gordon, 1998: Polarimetric method for ice water content determination. *Journal of Applied Meteorology*, **37**, 125-134.
- Ryzhkov, A. V., T. J. Schuur, D. W. Burgess, and D. S. Zrnica, 2005: Polarimetric tornado detection. *J. Appl. Meteor.*, **44**, 557-570.
- Vivekanandan, J., W. M. Adams, and V. N. Bringi, 1991: Rigorous approach to polarimetric radar modeling of hydrometeor orientation distributions. *J. Appl. Meteor.*, **30**, 1053-1063.
- Vivekanandan, J., V. N. Bringi, M. Hagen, and G. Zhang, 1994: Polarimetric radar studies of atmospheric ice particles. *IEEE Trans. Geosci. Remote Sens.*, **32**, 1-10.
- Wakimoto, R. M. and V. N. Bringi, 1988: Dual-polarization observations of microbursts associated with intense convection: The 20 July storm during the MIST Project. *Mon. Wea. Rev.*, **116**, 1521-1539.
- Walko, R. L., W. R. Cotton, M. P. Meyers, and J. L. Harrington, 1995: New RAMS cloud microphysics parameterization. Part I: The single-moment scheme. *Atmos. Res.*, **38**, 29-62.
- Waterman, P. C., 1969: Scattering by dielectric obstacles. *Alta Frequenza*, (Speciale), 348-352.
- Weisman, M. L. and J. B. Klemp, 1982: The dependence of numerically simulated convective storms on vertical wind shear and buoyancy. *Mon. Wea. Rev.*, **110**, 504-520.
- Xue, M., 2000: High-order monotonic numerical diffusion and smoothing. *Mon. Wea. Rev.*, **128**, 2853-2864.
- Xue, M., K. K. Droegemeier, and V. Wong, 2000: The Advanced Regional Prediction System (ARPS) - A multiscale nonhydrostatic atmospheric simulation and prediction tool. Part I: Model dynamics and verification. *Meteor. Atmos. Phys.*, **75**, 161-193.

- Xue, M., M. Tong, and K. K. Droegemeier, 2006: An OSSE framework based on the ensemble square-root Kalman filter for evaluating impact of data from radar networks on thunderstorm analysis and forecast. *J. Atmos. Ocean Tech.*, **23**, 46–66.
- Xue, M., Y. Jung, and G. Zhang, 2007: Error modeling of simulated reflectivity observations for ensemble Kalman filter data assimilation of convective storms. *Geophys. Res. Letters*, **34**, L10802, doi:10.1029/2007GL029945.
- Xue, M., M. Tong, and G. Zhang, 2009: Simultaneous state estimation and attenuation correction for thunderstorms with radar data using an ensemble Kalman filter: Tests with simulated data. *Q. J. Roy. Meteor. Soc.*, Conditionally accepted.
- Xue, M., D.-H. Wang, J.-D. Gao, K. Brewster, and K. K. Droegemeier, 2003: The Advanced Regional Prediction System (ARPS), storm-scale numerical weather prediction and data assimilation. *Meteor. Atmos. Phy.*, **82**, 139-170.
- Xue, M., K. K. Droegemeier, V. Wong, A. Shapiro, K. Brewster, F. Carr, D. Weber, Y. Liu, and D.-H. Wang, 2001: The Advanced Regional Prediction System (ARPS) - A multiscale nonhydrostatic atmospheric simulation and prediction tool. Part II: Model physics and applications. *Meteor. Atmos. Phy.*, **76**, 143-165.
- Zhang, G., J. Vivekanandan, and E. Brandes, 2001: A method for estimating rain rate and drop size distribution from polarimetric radar measurements. *IEEE Trans. Geosci. Remote Sens.*, **39**, 830-841.

List of figures

Fig. 1. Reflectivity (thin solid contours and shading), perturbation potential temperature (dotted contours at 0.5 K intervals from - 0.5 K) and horizontal perturbation wind vectors (plotted every fourth grid point; m s^{-1}) at $z = 250$ m for the simulated storm using (a)-(d) SM and (e)-(h) DM microphysics schemes. AA' and BB' in (h) show the locations of the vertical cross-sections to be shown in Fig. 2 that pass through the updraft core (maximum vertical velocity).

Fig. 2. Vertical cross-sections of simulated (a) Z_{DR} (dB) along line AA' shown in Fig. 1h corresponding to $x = 38.2$ km and (b) K_{DP} (degree km^{-1}) along line BB' corresponding to $y = 32.2$ km, of the simulated supercell storm at 100 min. The 0°C isotherms are shown as thick black lines.

Fig. 3. (a)-(c) Z_{DR} (shading, dB) and reflectivity (solid contours at 15 dBZ intervals, starting at 10 dBZ), (d)-(f) K_{DP} (shading, degree km^{-1}) and perturbation horizontal wind vectors (plotted every other grid point; m s^{-1}), and (g)-(i) hail mixing ratio q_h (shading, g kg^{-1}) and rain mixing ratio q_r (solid contours at 1 g kg^{-1} intervals starting at 1 g kg^{-1}) at 3 km (left column), 4 km (central column), and 5 km (right column) height, at 100 min of simulated storm. The vertical velocity contours (dotted contours at 5 m s^{-1} interval starting at 10 m s^{-1}) are overlaid on each plot.

Fig. 4. Z_{DR} (shading), q_r (solid contours at 0.5 g kg^{-1} intervals, starting at 0.5 g kg^{-1}), and a) mean-mass diameter of rain drops D_{nr} (dotted black contours at intervals of 0.1 mm, starting at 0.1 mm) for SM and b) D_{nr} (intervals of 0.3 mm, starting at 0.3 mm) for DM at $z = 500$ m at 80 min of simulated storm.

Fig. 5. (a) Z_{DR} (shading), Z_H (solid contours at 15 dBZ intervals from 15 dBZ), q_h (dotted contours at 1.0 g kg^{-1} intervals from 0.5 g kg^{-1}), and D_{nr} (thick dashed contours at intervals of 0.6 mm, starting at 0.9 mm) at $z = 4 \text{ km}$, and (b) ρ_{hv} (shading and solid contours at 0.01 intervals starting at 0.98 and lower) and the ratio of rain-hail mixture to the sum of rain and dry hail mixing ratios (dotted contours at 0.1 intervals from 0.2) at $z = 3 \text{ km}$, at 80 min of simulated storm. Ring features are prominent at mid-levels.

Fig. 6. Simulated ρ_{hv} with size of melting hailstones for the fraction of water, $f_w = 0.45$ (dotted), 0.65 (solid), and dry hailstone (dashed).

Fig. 7. The hail signature as characterized by high Z_H (thin solid contours at 15 dBZ intervals, starting at 15 dBZ) and low Z_{DR} (shading, dB) at $z = 2.5 \text{ km}$ at 60 min of simulated storm. The hail mixing ratio is overlaid in thick dashed contours at 1 g kg^{-1} intervals starting at 1 g kg^{-1} .

Fig. 8. As in Fig. 5b, but for simulation using the observation operator of JZX08. The Mie scattering effect is not included in this simple version of emulator.

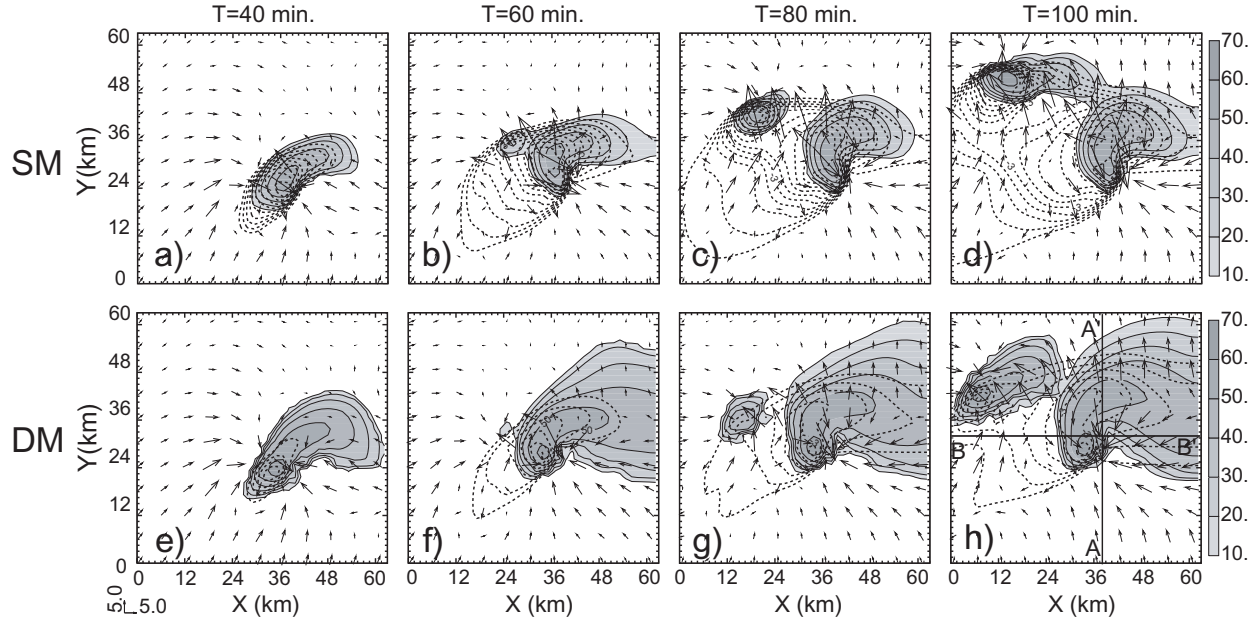


Fig. 1. Reflectivity (thin solid contours and shading), perturbation potential temperature (dotted contours at 0.5 K intervals from - 0.5 K) and horizontal perturbation wind vectors (plotted every fourth grid point; m s^{-1}) at $z = 250$ m for the simulated storm using (a)-(d) SM and (e)-(h) DM microphysics schemes. AA' and BB' in (h) show the locations of the vertical cross-sections to be shown in Fig. 2 that pass through the updraft core (maximum vertical velocity).

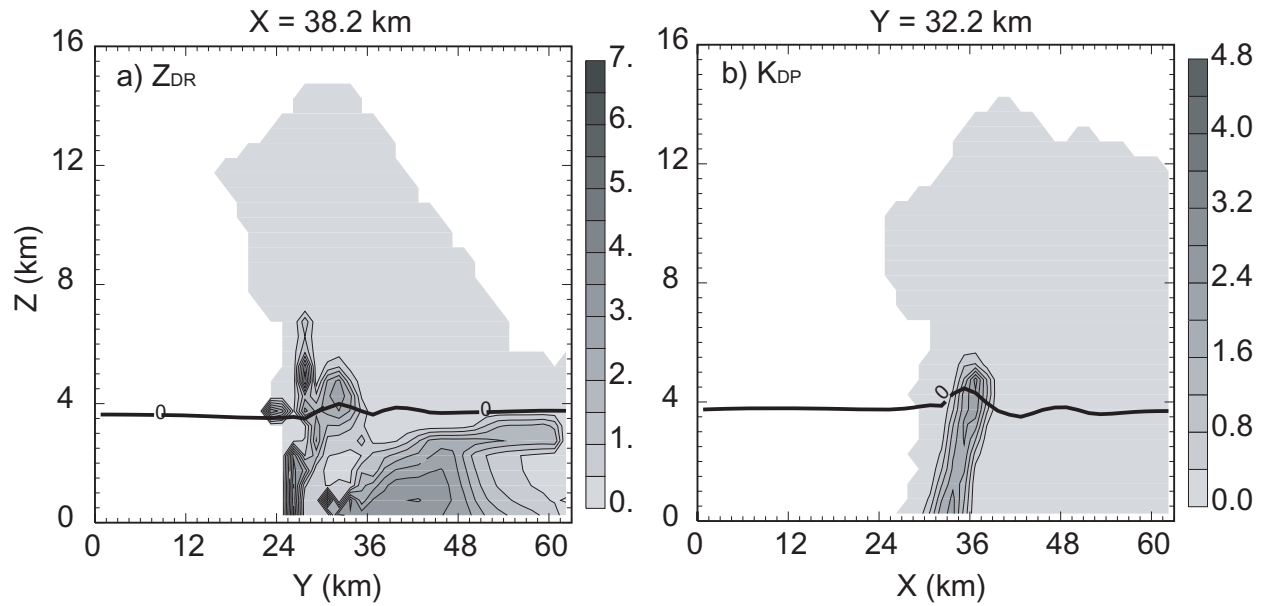


Fig. 2. Vertical cross-sections of simulated (a) Z_{DR} (dB) along line AA' shown in Fig. 1h corresponding to $x = 38.2$ km and (b) K_{DP} (degree km^{-1}) along line BB' corresponding to $y = 32.2$ km, of the simulated supercell storm at 100 min. The 0°C isotherms are shown as thick black lines.

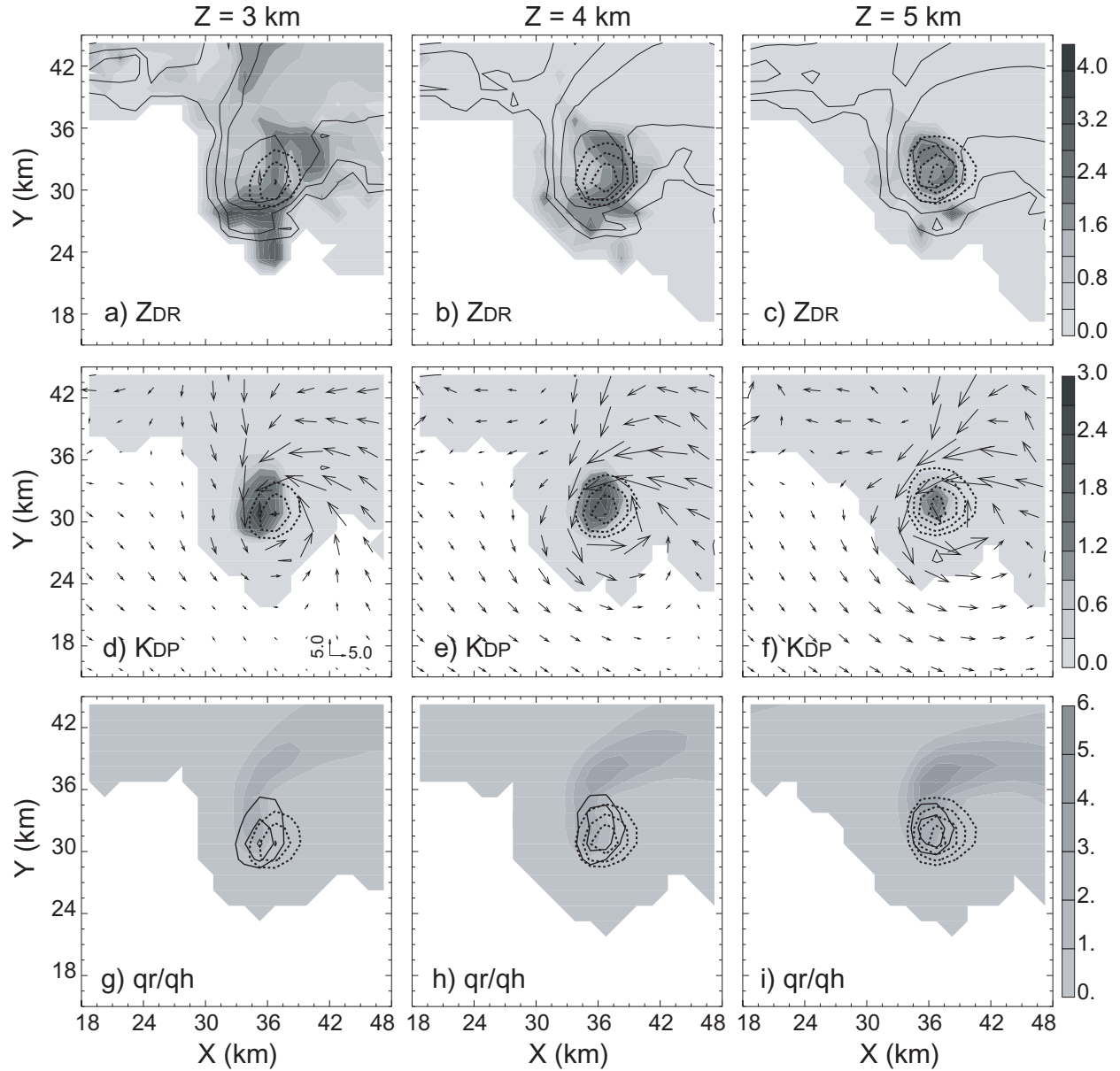


Fig. 3. (a)-(c) Z_{DR} (shading, dB) and reflectivity (solid contours at 15 dBZ intervals, starting at 10 dBZ), (d)-(f) K_{DP} (shading, degree km^{-1}) and perturbation horizontal wind vectors (plotted every other grid point; m s^{-1}), and (g)-(i) hail mixing ratio q_h (shading, g kg^{-1}) and rain mixing ratio q_r (solid contours at 1 g kg^{-1} intervals starting at 1 g kg^{-1}) at 3 km (left column), 4 km (central column), and 5 km (right column) height, at 100 min of simulated storm. The vertical velocity contours (dotted contours at 5 m s^{-1} interval starting at 10 m s^{-1}) are overlaid on each plot.

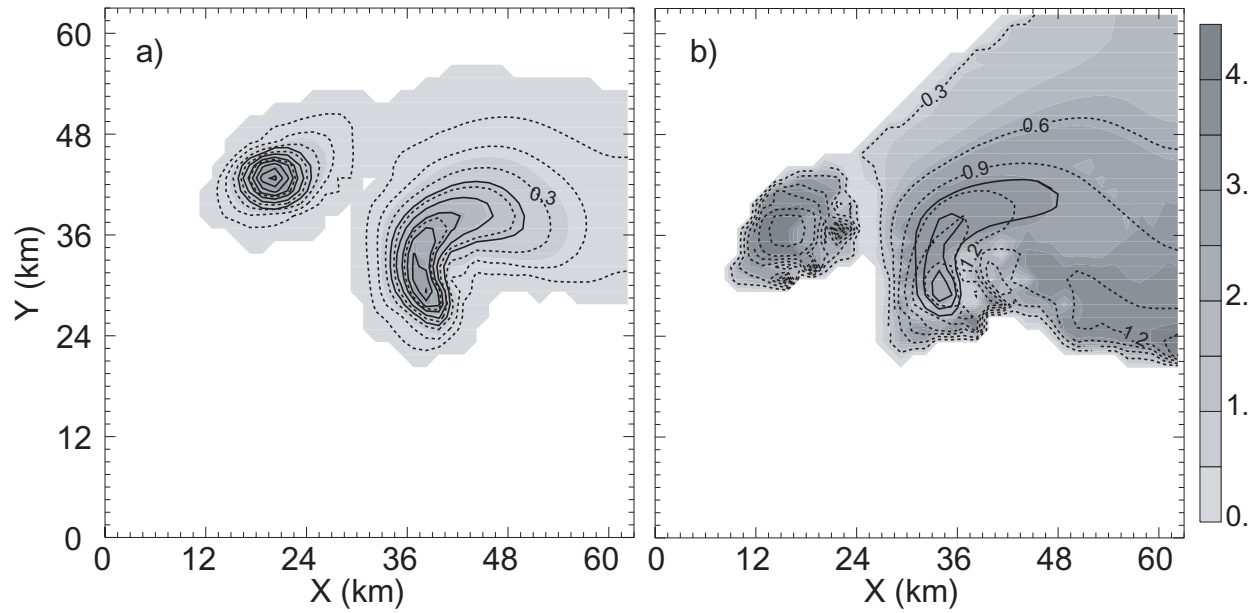


Fig. 4. Z_{DR} (shading), q_r (solid contours at 0.5 g kg^{-1} intervals, starting at 0.5 g kg^{-1}), and a) mean-mass diameter of rain drops D_{nr} (dotted black contours at intervals of 0.1 mm , starting at 0.1 mm) for SM and b) D_{nr} (intervals of 0.3 mm , starting at 0.3 mm) for DM at $z = 500$ m at 80 min of simulated storm.

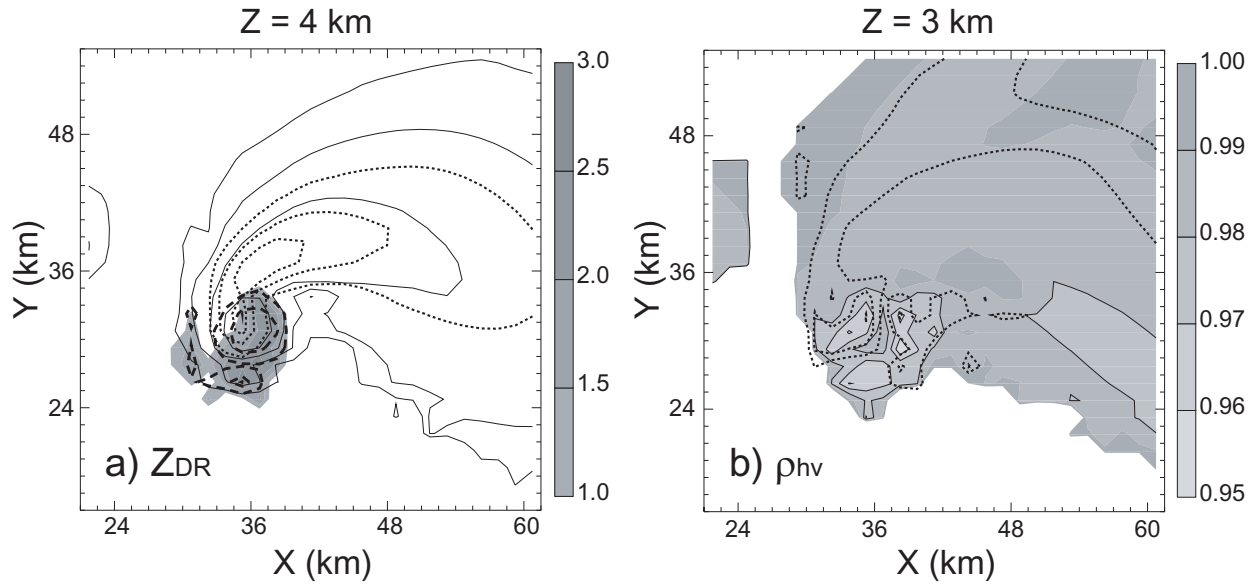


Fig. 5. (a) Z_{DR} (shading), Z_H (solid contours at 15 dBZ intervals from 15 dBZ), q_h (dotted contours at 1.0 g kg^{-1} intervals from 0.5 g kg^{-1}), and D_{nr} (thick dashed contours at intervals of 0.6 mm, starting at 0.9 mm) at $z = 4 \text{ km}$, and (b) ρ_{hv} (shading and solid contours at 0.01 intervals starting at 0.98 and lower) and the ratio of rain-hail mixture to the sum of rain and dry hail mixing ratios (dotted contours at 0.1 intervals from 0.2) at $z = 3 \text{ km}$, at 80 min of simulated storm. Ring features are prominent at mid-levels.

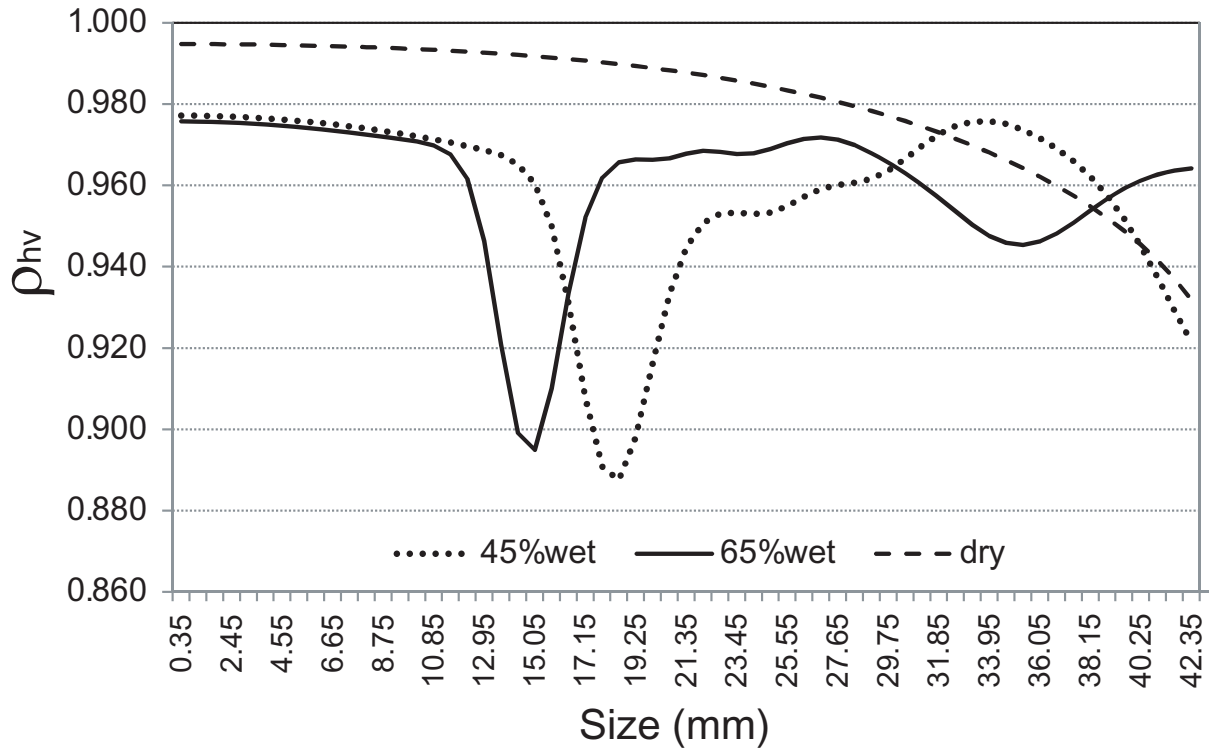


Fig. 6. Simulated ρ_{hv} with size of melting hailstones for the fraction of water, $f_w = 0.45$ (dotted), 0.65 (solid), and dry hailstone (dashed).

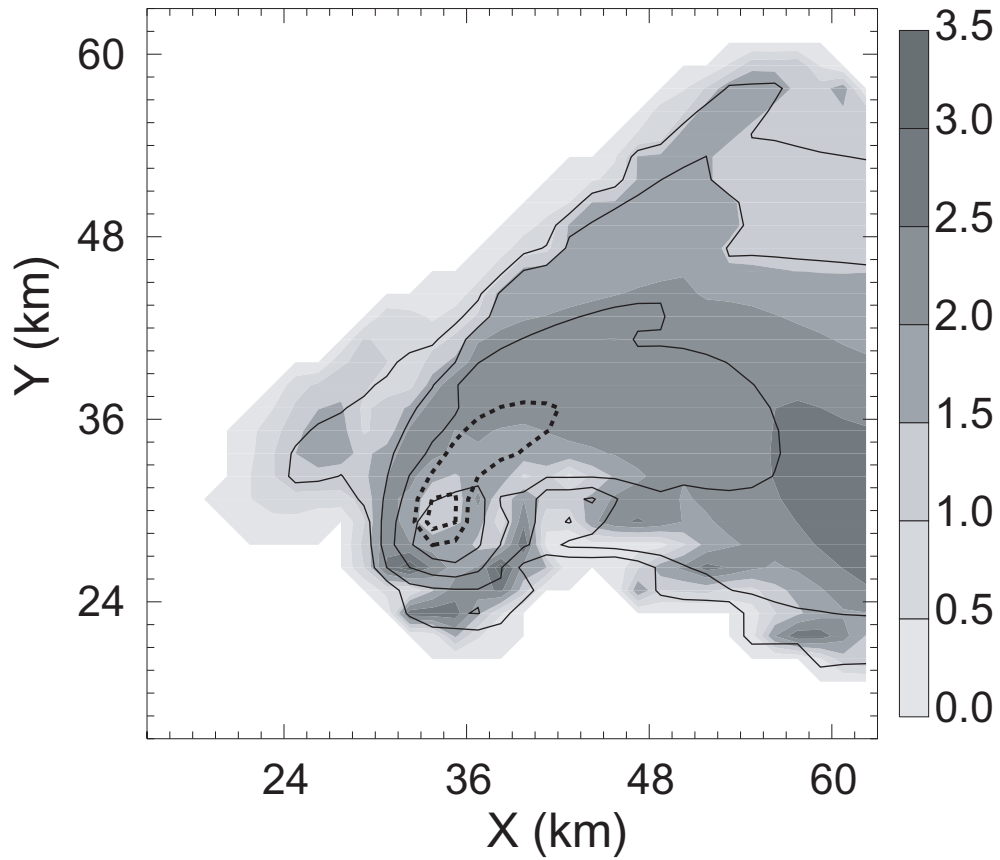


Fig. 7. The hail signature as characterized by high Z_H (thin solid contours at 15 dBZ intervals, starting at 15 dBZ) and low Z_{DR} (shading, dB) at $z = 2.5$ km at 60 min of simulated storm. The hail mixing ratio is overlaid in thick dashed contours at 1 g kg^{-1} intervals starting at 1 g kg^{-1} .

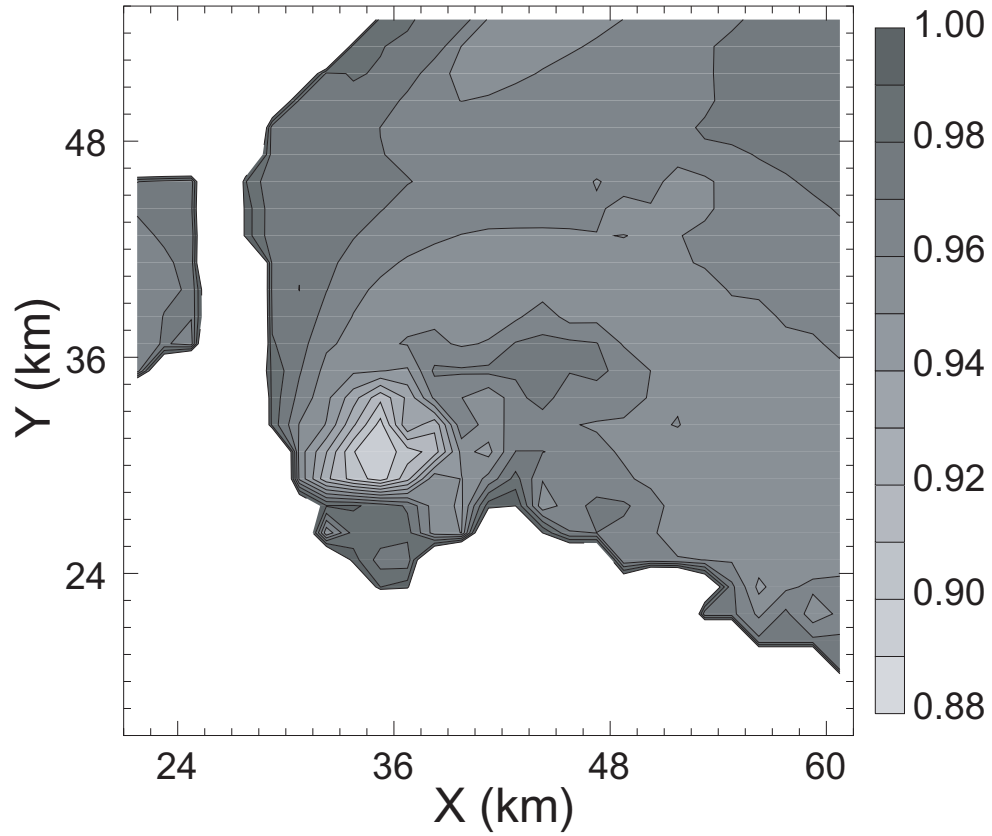


Fig. 8. As in Fig. 5b, but for simulation using the observation operator of JZX08. The Mie scattering effect is not included in this simple version of emulator.